Research Square

Preprints are preliminary reports that have not undergone peer review.
They should not be considered conclusive, used to inform clinical practice,
or referenced by the media as validated information.

Alterations of Choroid Plexus Hemodynamics in Pediatric Hydrocephalus: A Multi-delay Arterial Spin Labeling Study

Zibo Zhou
Second Affiliated Hospital & Yuying Children's Hospital of Wenzhou Medical University
Weizhi Xia
Second Affiliated Hospital & Yuying Children's Hospital of Wenzhou Medical University
Yunzhi Xu
Zhejiang University
Yubin Jin
Second Affiliated Hospital & Yuying Children's Hospital of Wenzhou Medical University
Peilong Pan
Second Affiliated Hospital & Yuying Children's Hospital of Wenzhou Medical University
Zixuan Lin
Zhejiang University
Dan Wu
Second Affiliated Hospital & Yuying Children's Hospital of Wenzhou Medical University
Zhihan Yan
Second Affiliated Hospital & Yuying Children's Hospital of Wenzhou Medical University
Li Zhao
lz5bf@virginia.edu

Zhejiang University

Research Article

Keywords: choroid plexus, hydrocephalus, arterial spin labeling, cerebral blood flow, arterial transit time

Posted Date: May 28th, 2026

DOI: https://doi.org/10.21203/rs.3.rs-9431924/v1

License: This work is licensed under a Creative Commons Attribution 4.0 International License.
Read Full License

Additional Declarations: No competing interests reported.

Alterations of Choroid Plexus Hemodynamics in Pediatric Hydrocephalus: A Multi-delay Arterial Spin Labeling Study

Zibo Zhou [1,3†], Weizhi Xia [1,3†], Yunzhi Xu [2], Yubin Jin [1,3], Peilong Pan [1,3], Zixuan Lin [2], Dan Wu [1,2], Zhihan Yan [1,3*], Li Zhao [2*]

1 Department of Radiology, The Second Affiliated Hospital and Yuying Children's Hospital of Wenzhou Medical University, Wenzhou, Zhejiang 325027, China.

2 Key Laboratory for Biomedical Engineering of Ministry of Education, College of Biomedical Engineering & Instrument Science, Zhejiang University, Hangzhou 310027, China

3 Wenzhou Key Laboratory of Structural and Functional Imaging, Wenzhou, 325027, China

†These authors contributed equally.

*Corresponding to

Zhihan Yan

Email: yanzhihanwz@163.com

Li Zhao

College of Biomedical Engineering & Instrument Science

86 Zheda Road, Hangzhou, Zhejiang, China, 310027

Email: lz5bf@virginia.edu

Phone: +86-130-949-00529

Abstract

Background: Choroid plexus (ChP) is the primary organ producing cerebrospinal fluid (CSF). Therefore, the increased CSF accumulation in hydrocephalus can be associated with the hemodynamic changes in the ChP. The present work investigated the alternations of ChP blood flow in pediatric hydrocephalus in addition to anatomic changes.

Methods: Multi-delay pseudo-continuous arterial spin labeling (pCASL) magnetic resonance imaging is employed to characterize cerebral perfusion in children with hydrocephalus. 17 patients with secondary hydrocephalus (sPH), 14 patients with idiopathic hydrocephalus (iPH), and 15 healthy controls (HCs) are included retrospectively and are grouped according to hydrocephalus symptoms. Beyond the anatomic changes, the blood flow of the ChP is quantified using three ASL models. In addition, multivariable logistic regression and ROC analysis are performed to evaluate the performance of imaging features in predicting clinical symptoms.

Results: Beyond ventricle enlargements, significantly decreased CBF is found in the sPH group ($p < 0.05$), while significantly prolonged arterial transit time was found in the iPH group ($p < 0.05$) in the grey matter and white matter, compared to the HCs. In addition, the blood flow and arterial transit time are significantly associated with Charlson Comorbidity Index (CCI) scores ($p < 0.01$) and gait disturbances ($p < 0.05$), respectively. More importantly, both iPH and sPH group show significantly reduced blood flow in the ChP ($p < 0.05$), compared to the HCs. Furthermore, the blood flow of the ChP is associated with CCI scores significantly ($p < 0.01$) and exhibits superior performance in CCI prediction (AUC 0.85 with ChP CBF, $p < 0.001$, and AUC 0.86 with multivariable logistic regression model, $p < 0.001$), compared to conventional ventricle enlargements.

Conclusions: The present study found significant hemodynamic changes in the pediatric patients with hydrocephalus and demonstrated the potential role of choroid plexus in hydrocephalus diagnosis.

Keywords: choroid plexus, hydrocephalus, arterial spin labeling, cerebral blood flow, arterial transit time

BACKGROUND

Hydrocephalus is one of the most common indications for pediatric neurosurgical intervention (Muir et al., 2016). It is caused by an imbalance in cerebrospinal fluid (CSF) homeostasis, which leads to abnormal CSF accumulation and subsequent ventricular expansion (Kahle et al., 2024). Hydrocephalus can lead to elevated intracranial pressure (ICP), compression of the brain parenchyma, and a series of clinical symptoms, such as headaches, vomiting, and papilledema (Shimony et al., 2021). Etiologically, hydrocephalus can be classified into secondary hydrocephalus (sPH), which is caused by a distinct etiology, such as intracranial infection or hemorrhage, and idiopathic hydrocephalus (iPH), in which a definitive etiology cannot be identified even after a comprehensive evaluation (Seltzer et al., 2024).

Conventionally, hydrocephalus is diagnosed based on clinical history, physical examination, and morphological changes. Magnetic resonance imaging (MRI) and computed tomography (CT) images provide direct evidence of morphological changes such as enlargement of the ventricles and subarachnoid space, which can be quantified as the Evans index and the DESH index respectively (Nakajima et al., 2021; Park et al., 2021). However, variations in these morphological features have been reported across multiple demographics, including gender and age (Muangpaisan et al., 2025). More importantly, the morphological features typically manifest only after the hydrocephalus has progressed to a late stage, which may limit their performance as effective indicators of clinical symptoms (Park et al., 2021).

In contrast, hemodynamic changes of the brain may provide more sensitive indicators and could accurately reflect the severity of hydrocephalus (Rosu et al., 2025). However, only a limited number of studies reported such alterations (Park, 2022). One of the prominent findings in hydrocephalus is that the ICP may result in altered hemodynamic characteristics within the brain parenchyma.

Virhammar et al. and Yeom et al. reported reduced cerebral blood flow (CBF) in hydrocephalus patients, particularly in the periventricular white matter, using arterial spin labeling (ASL) MRI (Virhammar et al., 2017; Yeom et al., 2014). However, conflicting findings were also reported by Owler et al using the PET imaging, in which regional CBF reduction was found in the basal ganglia and thalamus, rather than the white matter (Owler et al., 2004). One possible reason for the above discrepancy is that blood flow is slowed in hydrocephalus patients. The longer arterial transit time (ATT) of hydrocephalus patients could result in an underestimation of CBF in single post label delay (PLD) ASL protocol (Golay & Ho, 2022).

Compared to the parenchyma, choroid plexus (ChP) is the primary organ responsible for CSF production, which may reflect the functional changes in patients with hydrocephalus with high sensitivity (Johanson et al., 2008). The ChP is located in the lateral, third, and fourth ventricles, composed of fenestrated capillaries and epithelial cells with tidy junctions. The production of CSF at the ChP is directly associated with the blood supply to the ChP (Eisma et al., 2023). Therefore, the accumulation of CSF in hydrocephalus could trigger feedback mechanisms affecting the production of CSF and the hemodynamic characteristics within the ChP, which may provide a novel indicator for the clinical evaluation of hydrocephalus. This is the primary hypothesis of this work. In addition, the ChP is also the primary site where the immune system enters the central nervous system (Zhu et al., 2018). Since sPH can be caused by intracranial hemorrhage or infection, the ChP may reveal early changes related to these etiologies and may provide unique indicators to differentiate sPH from iPH.

Based on these hypotheses, the present study investigates structural and hemodynamic alterations in pediatric hydrocephalus patients and healthy controls. Beyond the conventional structural changes, ChP volume was measured on MRI structural images. The blood flow of ChP was measured

using multi-PLD ASL, which is the recommended model for clinical studies and offers more accurate CBF and ATT quantification (Lindner et al., 2023)

METHODS

Subjects

This retrospective study was approved by the Institutional Review Board (IRB) of the Second Affiliated Hospital of Wenzhou Medical University (approval number: 2025-k-301-01) in accordance with the Declaration of Helsinki, with a waiver of written informed consent.

Between May and July 2025, a total of 53 patients under 18 years of age who were scheduled for clinical brain MRI examinations at the Second Affiliated Hospital of Wenzhou Medical University were selected. The inclusion criteria for this work were ventriculomegaly confirmed via cranial CT or MRI, characterized by progressive ventricular enlargement disproportionate to brain parenchymal volume, and corresponding clinical symptoms, such as headaches, vomiting, and increasing head circumference (Kahle et al., 2024). Of the 53 candidates, 22 were excluded due to excessive head motion artifacts, ineffective arterial spin labeling, or uncertain diagnosis of hydrocephalus (HP). Consequently, 31 patients were included in the final analysis, as shown in Figure 1. Image quality assessment was performed by a neuroradiologist (Z.Z.) with 2 years of experience, and the results were subsequently validated by a neuroradiologist (Z.Y.) with 30 years of experience.

Based on clinical records and neuroimaging findings, the hydrocephalus patients were further divided into iPH and sPH subgroups. The iPH subgroup included patients with congenital morphological anomalies, such as aqueductal stenosis, Dandy-Walker malformations, and obstructive or non-obstructive hydrocephalus of unknown causes. The sPH subgroup included patients with acquired conditions, such as central nervous system (CNS) infections (e.g., bacterial meningitis), traumatic brain injury, and intracranial hemorrhage (e.g., periventricular, intraventricular, and subarachnoid hemorrhage).

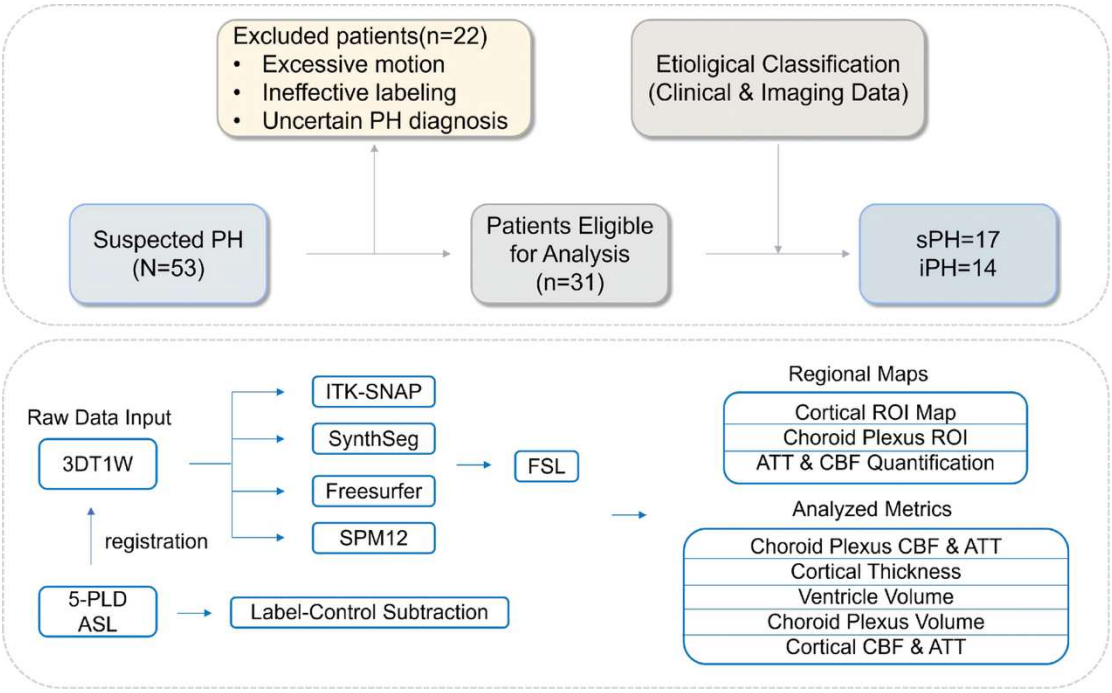


Figure 1. Study Flowchart and Image Processing Pipeline

The healthy controls (HCs) cohort was retrospectively selected from asymptomatic children who underwent brain MRI examinations at the health examination center of our hospital during the same period. Subjects in the HC group were matched to the patient group by age and sex. The inclusion criteria were an absence of morphological abnormalities or other significant findings on routine brain MRI, no history of neurological or psychiatric disorders in their medical records, and an absence of clinical symptoms related to elevated intracranial pressure or neurological dysfunction, such as headaches, vomiting, or abnormal increases in head circumference. The HC subjects were reviewed and selected by a neuroradiologist (Z.Z.) with two years of experience.

Clinical and Functional Assessment

Clinical and functional assessment data were extracted from the medical records. These assessments were conducted in accordance with the methodology described according to Leary et al. (Leary et al., 2024). In contrast to the total dementia often observed in adult patients, pediatric hydrocephalus typically manifests as subtler deficits in attention and memory (Deopujari et al.,

2021). To improve the sensitivity of the cognitive assessment, the traditional binary clinical assessment was modified to distinguish between present or absent cognitive impairment only and refined it into a four-level scale, including normal, inattentiveness, memory impairment, and cognitive dysfunction with scores of from 0 to 3 accordingly. The global functional disability was evaluated using the Modified Rankin Scale (mRS), which utilizes a seven-level scale, ranging from 0 (no symptoms) to 5 (severe disability) and 6 (unable to determine) (van Swieten et al., 1988). Patients with incomplete clinical records were marked as “unable to determine” and were excluded from average score calculations. The comorbidity burden was evaluated using the Charlson Comorbidity Index (CCI) (Charlson et al., 2022). The index attaches weighted scores (1, 2, 3, or 6) based on clinical severity. These individual weights were summed to generate a total CCI score, reflecting the patient's overall comorbidity burden. For example, in hydrocephalus patients, comorbid diabetes adds 1 point, while hemiplegia adds 2 points. Gait function was scored on an 8-level scale in which a score of 1 represents normal and. a score of 8 represents wheelchair dependency. Urinary function was scored on a 6-level scale, in which a score of 1 represents normal and a score of 6 represents bladder or bowel incontinence (Leary et al., 2024).

Hydrocephalus patients may show normal results in some clinical assessments. To account for this variation, subjects were categorized into two groups, ‘normal’ and ‘impaired’, based on each of their clinical assessment including gait, cognition, urinary, mRS, and CCI, similar to the dichotomization approach used by Cho et al. previously (Cho et al., 2025). Specifically, patients with gait impairment with a gait score ≥ 2, cognitive impairment with a cognitive score ≥ 1, urinary incontinence with a urinary score ≥ 2, functional disability with an mRS score ≥ 1, and comorbidity burden with a CCI score ≥ 1 were included into impaired groups. Otherwise, subjects with a lower score were considered as normal groups.

Magnetic Resonance Imaging Protocol

All MR images were acquired using a 3.0 T scanner (uMR 880, United Imaging Healthcare, Shanghai, China). 3D pseudo-Continuous Arterial Spin Labeling (pCASL) images were acquired using a multi-delay scheme to ensure accurate quantification of CBF and ATT. The pCASL image was acquired with the following parameters, a total scan time of 7 min 24 s, a repetition time (TR) of 6186 ms, an echo time (TE) of 14.02 ms, a field of view (FOV) of 224 mm × 224 mm, a voxel size of 3.5 mm × 3.5 mm × 3.5 mm, and 46 axial slices with a slice thickness of 3.5 mm. The labeling duration was 1800 ms and the PLDs were 500 ms, 1000 ms, 1500 ms, 2000 ms and 2500 ms with 2, 2, 2, 2, and 3 averages respectively.

T1-weighted (T1W) images were acquired using the MPRAGE sequence to provide morphological information, with a scan time of 3 min 46 s, a TR of 6.6 ms, a TE of 2.3 ms, and an inversion time of 1000 ms. The excitation flip angle was 8 degrees, an FOV of 256 mm × 240 mm, a voxel size of 0.8 mm × 0.8 mm × 0.8 mm, a slice thickness of 0.85 mm with no gap, and a total of 208 slices.

Morphological Features Extraction

T1W images were segmented by SPM12 toolbox to obtain the GM and WM masks (Statistical Parametric Mapping, version 12, Wellcome Centre for Human Neuroimaging, University College London, London, UK) (Ashburner & Friston, 2005). To ensure segmentation accuracy, all GM and WM segmentation masks were reviewed by a neuroradiologist (Z.Z., 2 years of experience) to align with anatomical all GM and WM surfaces on T1W images. Furthermore, the ventricles were segmented using the SynthSeg software (Billot et al., 2023), which provide six ventricular substructures, including the left and right lateral ventricles, the third ventricle, the fourth ventricle, and the left and right temporal horns. The volume of each ventricular component and

the total ventricular volume were calculated using the fslstats command within the FSL toolbox (version 6.0, FMRIB Centre, University of Oxford, Oxford, UK) (Jenkinson et al., 2012). In addition, cortical thickness was calculated using the recon-all command of the FreeSurfer (version 7.3.0, Martinos Center for Biomedical Imaging, Boston, MA, USA) (Fischl, 2012).

Functional Features Extraction

Choroid Plexus ROI

The bilateral ChP was manually delineated by a neuroradiologist (Z.Z.) with two years of experiences on the T1W images using ITK-SNAP software (version 3.8.0, Penn Image Computing and Science Laboratory, University of Pennsylvania, Philadelphia, PA, USA) (Yushkevich et al., 2006). To spatially align the functional and structural images, the ASL-derived maps were registered to the T1W image space using SPM12 toolbox.

Single Delay Blood Flow Model

To compared to previous works, CBF maps measured from a single PLD measurement using the following equation, as mentioned in previous works (Virhammar et al., 2017; Yeom et al., 2014).

$$\Delta M = \frac{2M_t^0 \cdot \beta \cdot \alpha \cdot T_{1t} \cdot f \cdot e^{-w/T_{1a}} \cdot \left(1 - e^{-\tau/T_{1t}}\right)}{\lambda}$$

where, the ΔM is the acquired ASL signal, M_t^0 is the reference image, $\alpha = 0.75$ is the arterial blood labeling efficiency, $\beta = 0.8$ is the signal background suppression efficiency, $T_{1t} = 1.5s$ is the longitudinal relation time of the tissue, $T_{1a} = 1.66s$ is the longitudinal relation time of the blood, f is the blood flow in ml/100g/min, δ is the arterial transit time, and $\tau = 1800ms$ is the blood labeling duration. The selection of the PLD (w) followed the consensus by ASL white paper with a value of 1.5 s used specifically for children (Alsop et al., 2015).

Multi-delay Blood Flow Model

To accurately quantify the blood flow, both CBF and ATT were calculated using the weighted delay method following the approach described by Dai et al.'s work (Dai et al., 2012). A calibration curve was established using the multi-PLD ASL protocol according to the weighted delay equation below, which provides a monotonically increasing lookup table for ATT calibration and not sensitive to the CBF changes.

$$WD(\delta) = \frac{\sum_{i=1}^{5} w_i \, \Delta M(\delta, w_i)}{\sum_{i=1}^{5} \Delta M(\delta, w_i)}$$

$$\Delta M = \frac{2M_t^0 \cdot \beta \cdot \alpha \cdot T_{1t} \cdot f \cdot e^{-\delta/T_{1a}} \cdot \left(e^{-\max(w-\delta,0)/T_{1t}} - e^{-\max(\tau+w-\delta,0)/T_{1t}}\right)}{\lambda}$$

Based on this, a whole-brain ATT map was calculated on a voxel-wise basis and the final CBF map was quantified by averaging the ATT corrected CBF maps derived from all five delay times. This approach corrects the possible underestimation of CBF when ATT is longer than the PLD in the single delay protocols.

CSF Generation Model

To quantify the hemodynamic parameters of the ChP, a least-squares fitting model was employed to estimate the T1 relaxation time of the labeled blood, which may indicate the transit from the blood to the CSF (Zhao et al., 2020), in addition to the ATT and CBF mentioned above. The fitting algorithm utilized the equation presented above to calculate ChP hemodynamic parameters, using the following variable constraints: T1 value [1.5-4.2] s, ATT [0.7-3.0] s, and CBF [10-100 mL/100g/min] (Dai et al., 2012; Zhao et al., 2020). To quantitatively evaluate the goodness of fit, the coefficient of determination (R^2) was calculated for each fitting curve, with $R^2 > 0.7$ set as the threshold. Additionally, a neuroradiologist (Z.Z., 2 years of experience) visually checked the goodness of

fit for every curve. These were to make sure each fit was reasonable.

Statistical Analysis

All statistical analyses were conducted using the SPSS software (version 26.0, IBM Corp., Armonk, NY, USA), with $p < 0.05$ defined as statistically significant.

Mean CBF values for the GM, WM, and ChP were extracted by averaging voxel-wise values within masks segmented in the above section. The normality of data distribution was assessed using the Shapiro-Wilk test, while the homogeneity of variance was evaluated using Levene's test. Group comparisons for CBF and ATT were performed using the one-way analysis of variance (ANOVA) for normally distributed data with equal variances, the Welch's corrected ANOVA for data with unequal variances, and the Kruskal-Wallis H-test for non-normally distributed data. Based on the data distribution and variance characteristics, post-hoc analyses were performed using the Tukey's Honestly Significant Difference (HSD) test for equal variances, the Games-Howell for unequal variances, and the Dunn's test with Bonferroni correction for non-normally distributed data. Multicollinearity among independent variables was assessed using the Variance Inflation Factor (VIF), with $VIF < 5$ indicating the absence of significant multicollinearity. For hierarchical linear regression, the F-test was used to determine the significance of the models and the R-square change.

To compare the sPH and iPH subgroups, the independent samples t-test was performed for normal distribution and equal variances, the Welch's corrected t-test was performed for normally distributed data with unequal variances, and the non-parametric Mann-Whitney U-test was used for non-normal distributions.

Diagnosis Models

The binary classification method for clinical outcomes was consistent with the

criteria described in the ‘Clinical and Functional Assessment’ section. The variables showing a possible significance (p <0.1) in the univariable analysis were selected for inclusion in the final multivariable logistic regression model. All models were evaluated based on its overall significance and calibration. The overall significance of the model coefficients was assessed by the Omnibus test (p < 0.05 indicates statistical significance), while the Hosmer-Lemeshow test was used to evaluate the model’s calibration, with p > 0.05 indicating a good fitness between observed and predicted outcomes.

Receiver operating characteristic (ROC) curves were generated to evaluate the performance of imaging features in predicting clinical symptoms, such as the presence of CCI, gait disturbances, and cognition dysfunction. The binary classification method for clinical outcomes was described in the Clinical and Functional Assessment section. The discriminatory capacity was quantified using the area under the curve (AUC) with a 95% confidence interval (CI). The optimal cutoff values were determined by maximizing the Youden Index (YI). The statistical significance of the AUC was evaluated against the null hypothesis of AUC = 0.5. A two-side p < 0.05 was considered statistically significant.

RESULTS

Demographic and Clinical Data

A total of 31 hydrocephalus patients (17 sPH and 14 iPH) and 15 HCs were enrolled in this study. The demographic characteristics are summarized Table 1.

Table 1. Demographic of subjects.

	HCs (n=15)	sPH (n=17)	iPH (n=14)	p
Age	4.27 (±3.17)	8.81 (±5.97)	5.81 (±5.43)	0.127
BMI	16.90 (±3.59)	17.85 (±2.66)	17.41 (±2.34)	0.246
Sex (M/F)	9/6	12/5	9/5	0.818
Gait	1 (±0)	1.86 (±0.663)	1.25 (±0.463)	<0.001***
Cognition	0 (±0)	0.93 (±0.917)	0.38 (±0.518)	0.003**
Urinary	1 (±0)	1.14 (±0.535)	1.25 (±0.707)	0.501
CCI	0 (±0)	2 (±0.679)	0.25 (±0.707)	<0.001***
mRS	0 (±0)	0.5 (±0.65)	0 (±0)	0.007**

Significant differences are marked with *p < 0.05, **p < 0.01 and ***p < 0.001.

No significant differences were observed among the HCs, iPH, and sPH groups regarding Body Mass Index (BMI), sex distribution, or age. One-way ANOVA revealed Significant differences across several clinical assessments, including the gait score ($p < 0.001$), the cognition score ($p = 0.003$), the CCI ($p < 0.001$), and the mRS ($p = 0.007$). However, no significant difference was found in terms of the urinary function score.

The manually selected ChP regions for representative subjects are shown in Figure 2. High blood flow was observed within the ChP (highlighted by the arrows), which is associated with the generation of CSF and is consistent with previous study (Lee et al., 2022).

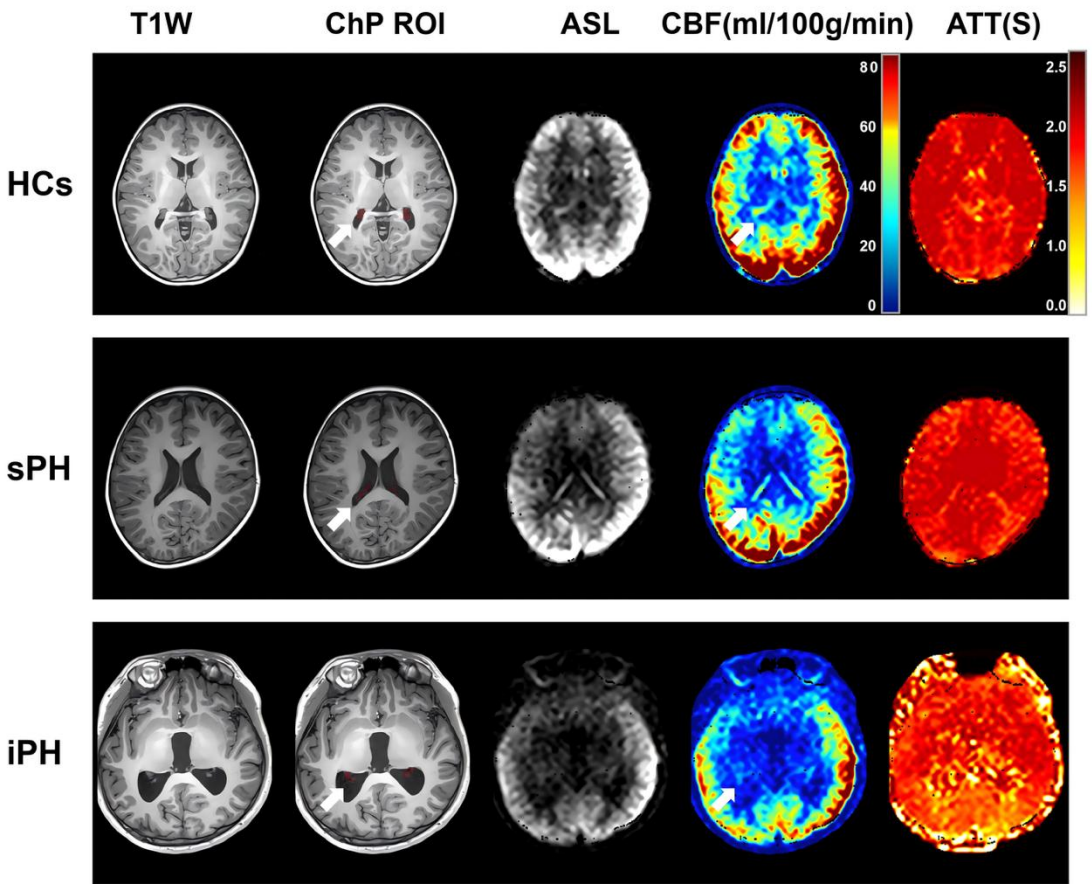


Figure 2. Manual segmentation of the choroid plexus and its perfusion maps.

Structural Changes in Hydrocephalus

Compared with the HC group, the Kruskal-wallis H-test shows that sPH and iPH groups have significant enlargements (p<0.01) in the left lateral ventricle (LLV), the right lateral ventricle (RLV), the third ventricle (3rdV), the inferior horn of the left lateral ventricle (LLV-IH), and the inferior horn of the right lateral ventricle (RLV-IH). Among these, the change in the total volume of ventricles (TVV) was the most prominent. Dunn's post hoc test reveals that the TVV volume in the sPH group is 59593.18 mm³ greater than that of the HC group (95% CI [24897.91, 94288.45] mm^3, p < 0.001), and the iPH group was 45172.46 mm³ greater than that of the HCs group (95% CI [19025.88, 71319.04] mm^3, p < 0.001). This finding is consistent with the results of Mortazavi et al. (Mortazavi et al., 2022). Additionally, Tukey's HSD post hoc test shows that the

left mean cortical thickness of the HCs group is 0.146 mm greater than that of the sPH group (95% CI [0.008, 0.284] mm, p = 0.036).

Furthermore, no statistically significant differences were observed in the ChP volume among the three groups. However, the Kruskal-wallis H-test shows a trend of increased ChP volume is found in the patients with hydrocephalus (1.26±0.28 cm^3 in HC, 1.55±0.43 cm^3 in sPH, and 1.44±0.39 cm^3 in iPH, p = 0.077) representing, as shown in Figure 3c.

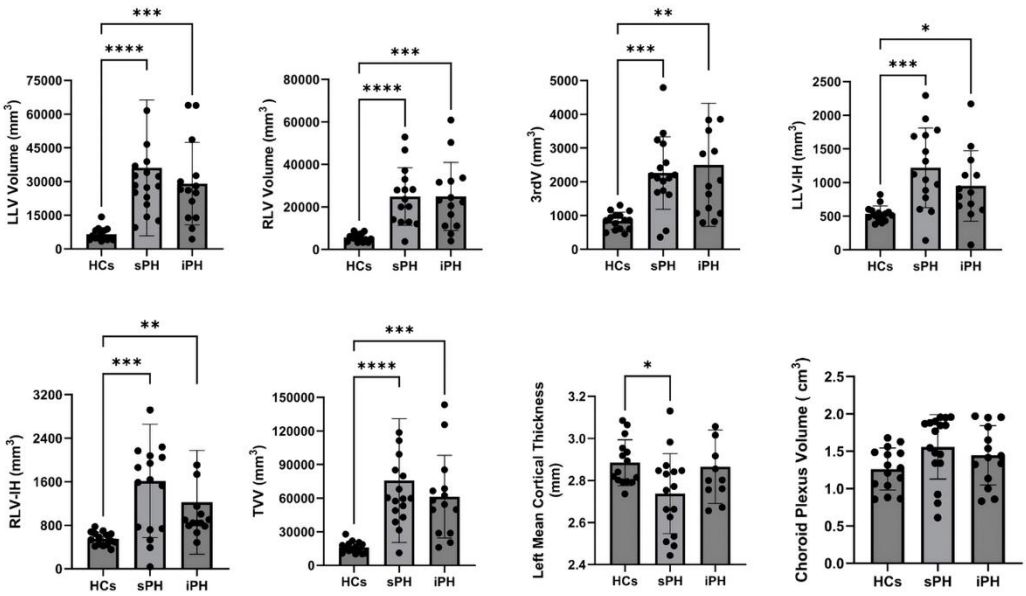


Figure 3. Brain structural differences among the HCs, sPH, and iPH groups. The left lateral ventricle (LLV), right lateral ventricle (RLV), third ventricle (3rdV), left temporal horn (LLV-IH), and right temporal horn (RLV-IH). Significant differences are marked with * p < 0.05, **p < 0.01, *** p< 0.001, and ****p < 0.0001.

TVV enlargement is associated with clinical assessment, and the Mann-Whitney U-test shows that its values are significantly greater (p < 0.05) in the patients with impaired gait, cognition and CCI groups compared to the patients with the normal scores in clinical assessments, as shown in Figure 4. These findings indicate associations between ventricular enlargement and clinical

symptoms, aligning with existing clinical expectations.

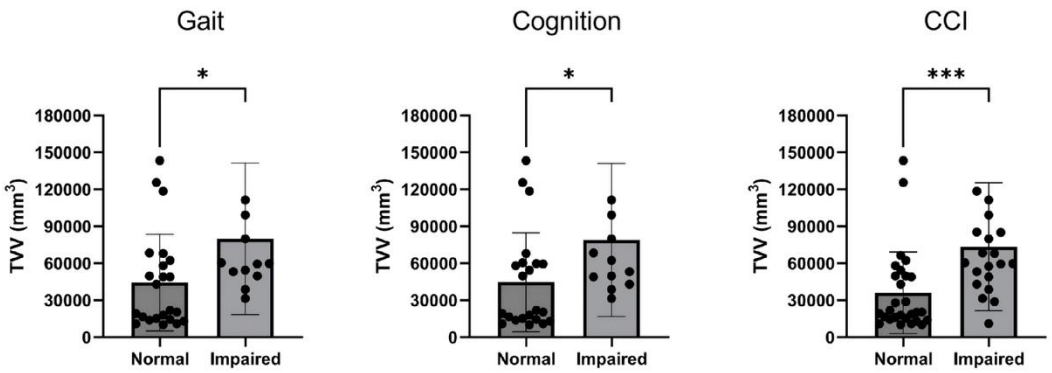


Figure 4. Relationship between brain structural metrics and clinical symptom severity. Significant differences are marked with *p < 0.05, **p < 0.01. ***p <0.001.

Single Delay Blood Flow Model

As shown in Figure 5, the CBF in the ChP is significantly higher in the HC group compared with both the sPH group and the iPH group (8.32±1.37 ml/100g/min in HC, 5.42±1.72 ml/100g/min in sPH (p < 0.001), and 6.04±1.67ml/100g/min in iPH (p < 0.01) in the Games-Howell post hoc test). However, no significant difference in the CBF of ChP was observed between the sPH and iPH groups. Our data did not show significant CBF difference in the GM and WM regions using the single-PLD model.

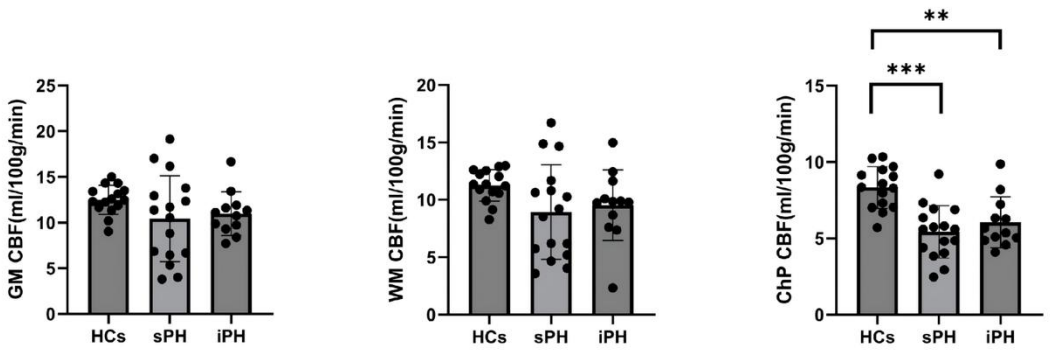


Figure 5. Hemodynamic changes from the single-PLD model in the

hydrocephalus patients. Significant differences are marked with ** p<0.01 and ***p<0.001.

Multi-Delay Blood Flow Model

As shown in Figure 6, the CBF of the ChP estimated using the multi-delay blood flow model was significantly higher in the HC group compared with both the sPH group and the iPH group (21.77±4.03 ml/100g/min in HC, 12.64±4.55 ml/100g/min in sHC (p < 0.001), and 16.37±7.39 ml/100g/min in iPH (p < 0.05) in the Tukey's HSD post hoc test and normal distribution). However, no significant difference in the CBF of ChP is observed between the sPH and iPH groups.

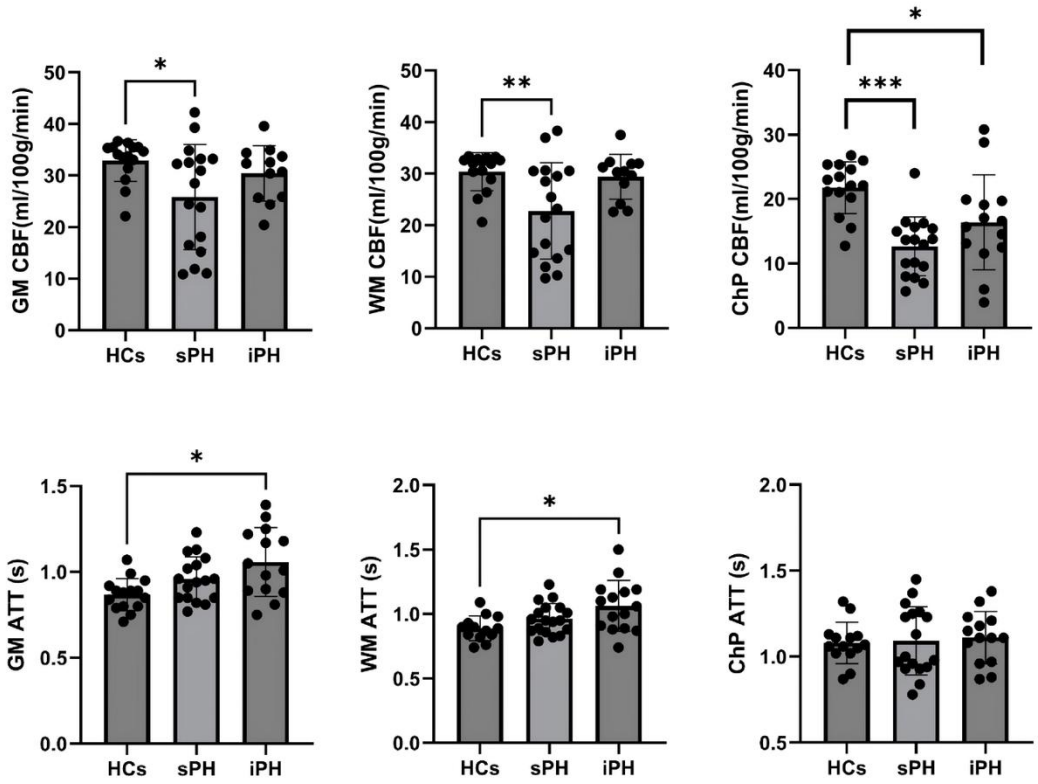


Figure 6. Hemodynamic changes from the multi-PLD model in the hydrocephalus patients. Significant differences are marked with * p < 0.05, **p < 0.01 and ***p < 0.001.

Additionally, the sPH group shows significantly lower CBF in the GM compared

to the HC group (34.06 [31.42–35.47] ml/100g/min in HC, 28.48 [15.85–33.23] ml/100g/min in sPH ($p < 0.05$) in the Dunn's post hoc test and non-normally distribution) and significantly reduced WM CBF (31.94 [28.90–32.86] ml/100g/min in HC, 23.18 [14.11–30.51] ml/100g/min in sPH ($p < 0.01$) in the Dunn's post hoc test and non-normally distribution). Furthermore, the ATT of the GM region in the iPH group is significantly longer than that of the HC group (0.86±0.024 s in HC, 1.05±0.053 s in iPH ($p = 0.003$) in the Games-Howell post hoc test) and significantly prolonged WM ATT (0.89±0.09 s in HC, 1.05±0.2 s in iPH ($p = 0.015$) in the Games-Howell post hoc test). Similarly, no significant difference in ATT was found between the sPH and HC group.

CSF Generation Model

As shown in Figure 7, in the CSF generation model, the ChP CBF is significantly reduced in both the sPH group and the iPH group, compared to the HCs (54.46 [43.31–61.17] ml/100g/min in HC, 29.13 [22.99–38.38] ml/100g/min in sPH ($p < 0.001$), and 30.36 [19.72–34.74] ml/100g/min in iPH ($p < 0.001$), in the Dunn's post hoc test). No significant difference in ChP ATT and T1 Value was found between the three groups.

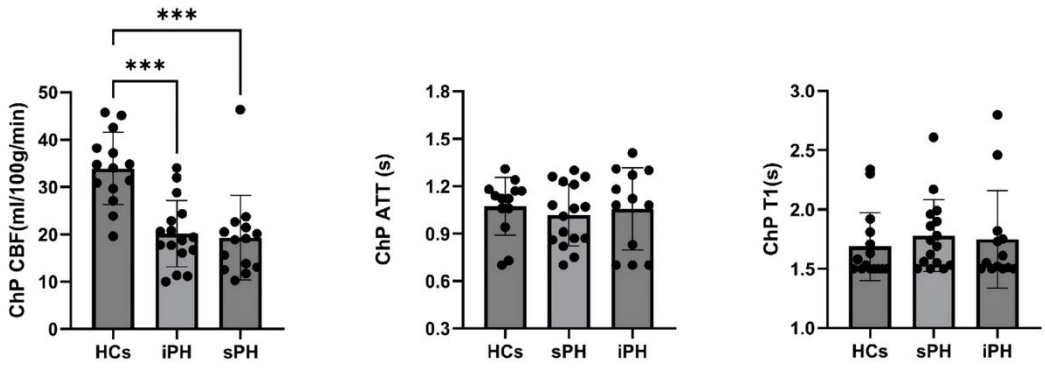


Figure 7. Hemodynamic changes from the CSF-Generation Model in the hydrocephalus patients. Significant differences are marked with * $p < 0.05$ and ** $p < 0.01$. *** $p < 0.001$

Hemodynamic Changes Related to Clinical Symptoms

The CBF of the ChP, GM, WM, and the cortical ATT, estimated using the multi-delay blood flow model, were significantly associated with patients' clinical symptoms, as shown in Figure 8. Specifically, analysis using the Mann-Whitney U-test revealed that the CBF in the ChP, GM, and WM is significantly associated with CCI ($p < 0.01$ for all). Furthermore, based on Welch's t-test, patients with impaired gait exhibited significantly prolonged GM and WM ATT values than the patients with normal scores ($p = 0.032$ and 0.026). The detailed statistical data and corresponding figures for these non-significant results are provided in the Appendix S1.

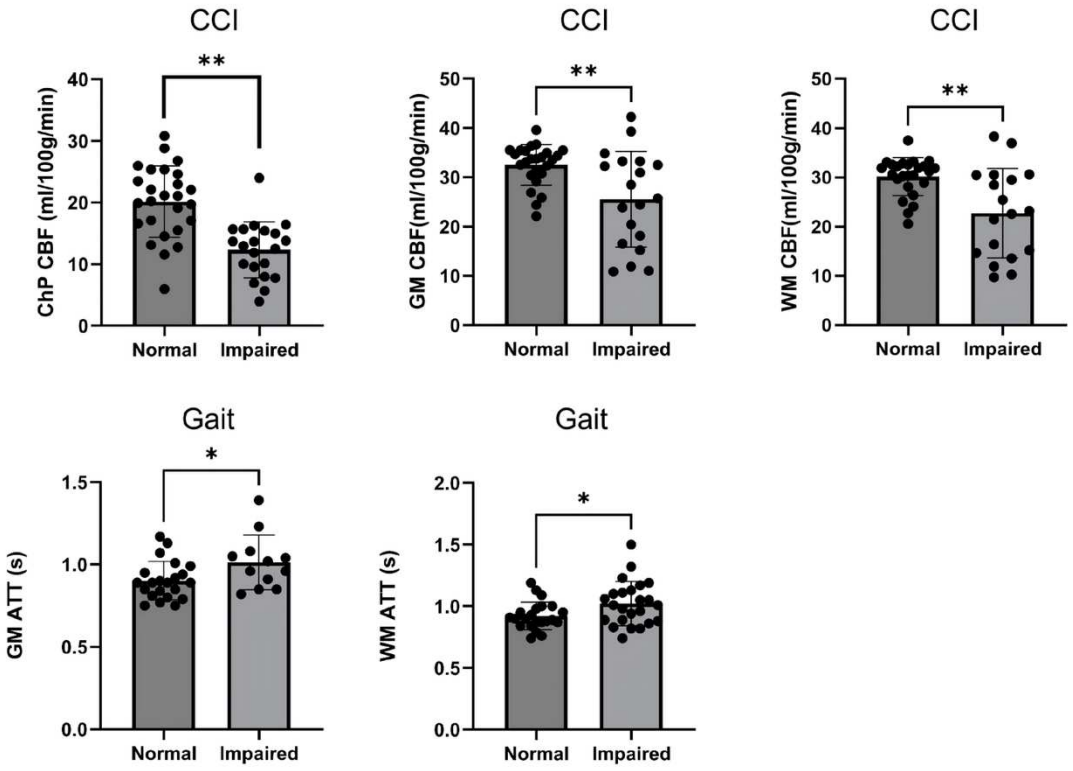


Figure 8. The relationship between cerebral hemodynamic metrics and clinical symptom severity. Significant differences are marked with *$p < 0.05$, **$p < 0.01$.

Predictive Performance for CCI

The results of the ROC curve analysis for predicting the presence of CCI are

shown in Figure 9 and Table 2. Ventricle enlargement and the CBF of parenchyma shows significant effects in the prediction of CCI. Especially, the CBF of ChP provided the best performance in predicting the CCI with an AUC of 0.88 (p < 0.001). Specifically, a lower ChP CBF was associated with a decreased risk of CCI in the multivariable logistic regression model (Adjusted OR = 0.791, 95% CI: 0.667-0.937, p = 0.007), as shown in Table 3.

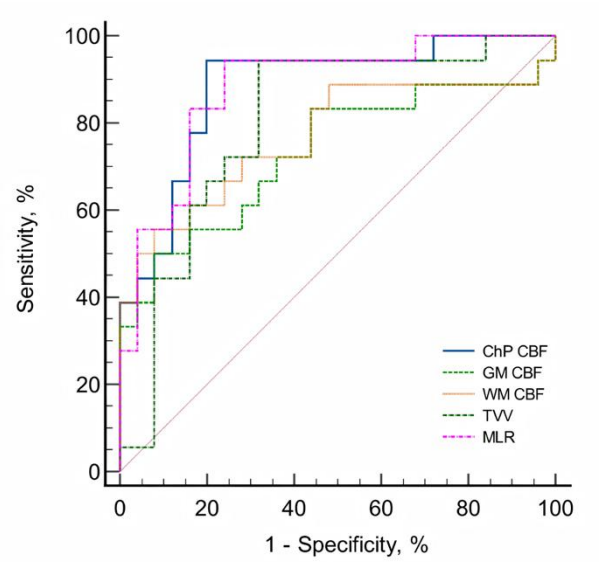


Figure 9. The ROC curves of imaging parameters for predicting the presence of CCI. MLR, the multivariable logistic regression model including ChP CBF, age, sex, and TVV as independent variables.

Table 2. Diagnostic effectiveness of the imaging features for predicting the presence of CCI

	AUC (95% CI)	Cutoff	Sensitivity	Specificity	YI	*p* (Omnibus)	*p* (H-L)
TVV	0.81 (0.66-0.90)	27.90	**95%**	65%	0.60	0.002	0.099
GM CBF	0.75 (0.59-0.86)	25.70	53%	**92%**	0.45	0.002	0.326
WM CBF	0.77 (0.61-0.88)	23.18	56%	**92%**	0.48	0.001	0.297
GM ATT	0.63 (0.48-0.77)	0.91	70%	62%	0.32	0.196	0.428
WM ATT	0.62 (0.46-0.76)	0.94	70%	62%	0.32	0.418	0.392
ChP CBF	**0.85 (0.72-0.94)**	16.42	**95%**	77%	0.72	**<0.001**	0.377
MLR	**0.86 (0.72-0.94)**	/	**95%**	69%	0.64	**<0.001**	0.495

Note: AUC, Area Under the Curve; YI, Youden Index. *p* (Omnibus), Omnibus test; *p* (H-L), Hosmer-Lemeshow test; MLR, the multivariable logistic regression model including ChP CBF, age, sex, and TVV as independent variables.

Table 3. Multivariable logistic regression analysis for predicting the presence of CCI

	B	S.E.	Adjusted OR (95% CI)	*p*
ChP CBF	-0.230	0.087	0.79 (0.67-0.94)	**0.007**
TVV	-0.011	0.010	0.98 (0.97-1.00)	0.269
age	0.046	0.076	1.05 (0.90-1.21)	0.547
sex	0.121	0.864	1.12 (0.21-6.13)	0.889

Note: B, Regression coefficient; S.E., Standard Error; Adjusted OR, Odds Ratio adjusted for all variables in the table

DISCUSSION

The present study investigated hemodynamic changes in pediatric hydrocephalus beyond the conventional structural changes. Accurate CBF and ATT of the parenchyma and the choroid plexus were measured using a multi-PLD ASL protocol compared to previous studies. Hydrocephalus patients show significantly lower ChP CBF compared to the HC group, and this reduction is associated with gait disturbances and comorbidity burden significantly. In addition, sPH patients show significantly reduced CBF and iPH patients show significantly prolonged ATT in the parenchyma, compared to the HCs, which are correlated with gait and CCI impairment. Furthermore, the blood flow of the ChP provided high performance in the CCI prediction.

The hemodynamic changes estimated through multi-PLD ASL model, including reduced CBF and prolonged ATT reveal the additional indicators of hydrocephalus. Ventricular enlargement or ventriculomegaly may exert mechanical compression on the surrounding brain parenchyma, thereby leading to decreased brain compliance. Such changes will directly affect the amount of blood flow and its transit time. In this study, reduced CBF measured by the multi-PLD ASL model was found in GM region, which is consistent with previous works. For example, Lokossou et al., using intracranial pressure monitoring combined with phase-contrast MRI, assessed ventricular compliance and found it to significantly lower than expected levels in hydrocephalus patients, and Portella et al. found that decreased brain compliance is strongly associated with cerebral hypoperfusion (Lokossou et al., 2018; Portella et al., 2005). In addition, as shown in the result section, the combination of conventional anatomic changes and functional changes provided improved power to explain pathophysiological mechanism of hydrocephalus.

The CBF of ChP region provide essential information related to CSF production and the cause of the hydrocephalus. As the major organ of CSF production, the reduced CBF in the ChP was found in all three models mentioned in this work including the single-PLD, multi-PLD, and CSF-generation models. The reduced blood flow can be related to the reduced CSF generation, which can be a negative feedback mechanism of hydrocephalus. In addition, emerging evidence suggests that neuroinflammation plays a key role in the pathology of ventricular enlargement (Espinoza-Vinces et al., 2025). As mentioned by Wang et al, multiple inflammatory mediators can be detected in the CSF of hydrocephalus patients, which supports above claim (Wang et al., 2020). As highlighted by Wang et al., the ChP acts as a key entry point for immune cells to enter the brain during injury or infection (Kaur et al., 2016). Consequently, the ChP itself is inevitably involved in the neuroinflammatory response. It is possible that the ChP requires less energy due to its functional damage. The combination of the above two effects may lead to the decreased CBF in ChP, which is worthy further investigation.

This work measured the ATT of pediatric hydrocephalus cohort accurately using a multi-delay ASL protocol and provide extra hemodynamic information. Although the changes of CBF have been reported in Virhammar, J. works, the CBF was measured using a single delay ASL protocol, which may underestimated the CBF when the arterial transit time is longer than the post labeling delay (Virhammar et al., 2017). Therefore, the findings of single-PLD in Ho et al's work cannot distinguish the possible dysfunction related to the CBF and ATT. The proposed method employed a multi-PLD protocol, which can image the process of arterial blood flow in and flow out, and therefore, provide more accurate measurements of the blood flow (Dai et al., 2012). The prolonged ATT and significantly reduced CBF in both the GM and WM regions, as measured by the multi-PLD ASL model in this work, Fig. 6, may describe an

increased resistance of brain as described by Greitz in which hydrocephalus amplifies mechanical stress compressed vessels and directly leads to increased cerebrovascular resistance (Greitz, 2004) because of the increased cerebrovascular resistance and cerebral hypoperfusion. The result provides a potential indicator of idiopathic and secondary etiologies and uncovering an unprecedented association between ChP perfusion and gait disturbance.

ROC curve analysis revealed that functional imaging features exhibited high diagnostic accuracy for predicting the presence of CCI. Notably, the functional perfusion marker ChP CBF demonstrated superior predictive performance compared to the traditional structural marker TVV. This finding suggests that ChP CBF may serve as a functional indicator for quantifying clinical severity, as complementing the traditional structural measurements, such as TVV.

Although no direct significant difference was found between the sPH and iPH groups, the sPH and iPH showed different changes related to control groups. Compared to the HCs, the anatomic changes in the sPH are more sever, including larger LLV, LLV-IH, RLV-IH, TVV, and ChP volume. In addition, the cortical thickness and the blood flow of the ChP are reduced more in the sPH, compared to the iPH, as shown in Fig. 3 and Fig. 6. In the hemodynamic measurements, the sPH also shows significantly reduced CBF, while iPH shows significantly prolonged ATT in GM and WM, as shown in Fig. 6. These findings could be partly explained by the infection in sPH. However, current findings are not sufficient to distinct the two based on MR images.

Nevertheless, several limitations of the present work must be considered. First, the sample size for each group was relatively modest, which may limit statistical power and required us to dichotomize clinical scores for correlation analyses, potentially masking true dose-response relationships. Second, the lack of longitudinal data. Specifically, the current design prevents us from establishing

an early hydrocephalus indicator. Although blood flow issues were supposed to appear before the ventricles enlarge, but it cannot be confirmed in current data. It would be worthy to validate the prediction of shunt surgery response with longitudinal follow up. Third, the sPH group as mentioned in the introduction includes many different causes, because the sample was not enough, we could not do a more detailed analysis on these subgroups. Fourth, the dominate handedness was not recorded in this study and it is unclear whether the left-sided changes are associated with hemispheric dominance. Finally, the wide age range of our cohort is a potential confounder. CBF is known to vary significantly with age. Although the age difference between groups was not significant in this study, it would be interesting to confirm current hemodynamic findings in the elderly group.

CONCLUSIONS

This work studies the hemodynamic changes in pediatric hydrocephalus using the multi-PLD ASL protocol and found significant alternations in the blood flow of ChP and the parenchyma, compared to the control group. Notably, these hemodynamic metrics demonstrated significant correlations with clinical assessments, such as gait disturbance and the CCI. These findings provide potential indicators of the pathophysiological mechanisms of hydrocephalus and could serve as promising models helping the evaluation of hydrocephalus.

REFERENCES

Alsop, D. C., Detre, J. A., Golay, X., Gunther, M., Hendrikse, J., Hernandez-Garcia, L., Lu, H., MacIntosh, B. J., Parkes, L. M., Smits, M., van Osch, M. J., Wang, D. J., Wong, E. C., & Zaharchuk, G. (2015). Recommended implementation of arterial spin-labeled perfusion MRI for clinical applications: A consensus of the ISMRM perfusion study group and the European consortium for ASL in dementia. *Magn Reson Med*, *73*(1), 102-116. https://doi.org/10.1002/mrm.25197

Ashburner, J., & Friston, K. J. (2005). Unified segmentation. *Neuroimage*, *26*(3), 839-851. https://doi.org/10.1016/j.neuroimage.2005.02.018

Billot, B., Greve, D. N., Puonti, O., Thielscher, A., Van Leemput, K., Fischl, B., Dalca, A. V., Iglesias, J. E., & Adni. (2023). SynthSeg: Segmentation of brain MRI scans of any contrast and resolution without retraining. *Med Image Anal*, *86*, 102789. https://doi.org/10.1016/j.media.2023.102789

Charlson, M. E., Carrozzino, D., Guidi, J., & Patierno, C. (2022). Charlson Comorbidity Index: A Critical Review of Clinimetric Properties. *Psychother Psychosom*, *91*(1), 8-35. https://doi.org/10.1159/000521288

Cho, H. J., Kim, S., Yu, H., Jeong, S., & Kang, K. (2025). Quantitative analysis of gait and balance using deep learning on monocular videos and the timed up and go test in idiopathic normal-pressure hydrocephalus. *Front Aging Neurosci*, *17*, 1644543. https://doi.org/10.3389/fnagi.2025.1644543

Dai, W., Robson, P. M., Shankaranarayanan, A., & Alsop, D. C. (2012). Reduced resolution transit delay prescan for quantitative continuous arterial spin labeling perfusion imaging. *Magn Reson Med*, *67*(5), 1252-1265. https://doi.org/10.1002/mrm.23103

Deopujari, C., Mohanty, C., Agrawal, H., Jain, S., & Chawla, P. (2021). A comparison of Adult and Pediatric Hydrocephalus. *Neurol India*, *69*(Supplement), S395-S405. https://doi.org/10.4103/0028-3886.332283

Eisma, J. J., McKnight, C. D., Hett, K., Elenberger, J., Song, A. K., Stark, A. J., Claassen, D. O., & Donahue, M. J. (2023). Choroid plexus perfusion and bulk cerebrospinal fluid flow across the adult lifespan. *J Cereb Blood Flow Metab*, *43*(2), 269-280. https://doi.org/10.1177/0271678X221129101

Espinoza-Vinces, C., Aviles-Olmos, I., Nunez-Cordoba, J. M., Jimenez-Vazquez, M., Calvo-Imirizaldu, M., Montoya-Murillo, G., Marti-Andres, G., Arbizu, J., & Luquin, M. R. (2025). Peripheral immunity patterns, imaging features, and clinical outcomes in patients with gait impairment and ventriculomegaly on brain MRI. *Front Aging Neurosci*, *17*, 1685288. https://doi.org/10.3389/fnagi.2025.1685288

Fischl, B. (2012). FreeSurfer. *Neuroimage*, *62*(2), 774-781. https://doi.org/10.1016/j.neuroimage.2012.01.021

Golay, X., & Ho, M. L. (2022). Multidelay ASL of the pediatric brain. *Br J Radiol*, *95*(1134), 20220034. https://doi.org/10.1259/bjr.20220034

Greitz, D. (2004). Radiological assessment of hydrocephalus: new theories and implications for therapy. *Neurosurg Rev*, *27*(3), 145-165; discussion 166-147. https://doi.org/10.1007/s10143-004-0326-9

Jenkinson, M., Beckmann, C. F., Behrens, T. E., Woolrich, M. W., & Smith, S. M. (2012). Fsl. *Neuroimage*, *62*(2), 782-790. https://doi.org/10.1016/j.neuroimage.2011.09.015

Johanson, C. E., Duncan, J. A., 3rd, Klinge, P. M., Brinker, T., Stopa, E. G., & Silverberg, G. D. (2008). Multiplicity of cerebrospinal fluid functions: New challenges in health and disease. *Cerebrospinal Fluid Res*, *5*, 10. https://doi.org/10.1186/1743-8454-5-10

Kahle, K. T., Klinge, P. M., Koschnitzky, J. E., Kulkarni, A. V., MacAulay, N., Robinson, S., Schiff, S. J., & Strahle, J. M. (2024). Paediatric hydrocephalus. *Nat Rev Dis Primers*, *10*(1), 35. https://doi.org/10.1038/s41572-024-00519-9

Kaur, C., Rathnasamy, G., & Ling, E. A. (2016). The Choroid Plexus in Healthy and Diseased Brain. *J Neuropathol Exp Neurol*, *75*(3), 198-213. https://doi.org/10.1093/jnen/nlv030

Leary, O. P., Zhong, Z., Bi, L., Jiao, Z., Dai, Y. W., Ma, K., Sayied, S., Kargilis, D., Imami, M., Zhao, L. M., Feng, X., Riccardello, G., Collins, S., Svokos, K., Moghekar, A., Yang, L., Bai, H., Klinge, P. M., & Boxerman, J. L. (2024). MRI-Based Prediction of Clinical Improvement after Ventricular Shunt Placement for Normal Pressure Hydrocephalus: Development and Evaluation of an Integrated Multisequence Machine Learning Algorithm. *AJNR Am J Neuroradiol*, *45*(10), 1536-1544. https://doi.org/10.3174/ajnr.A8372

Lee, H., Ozturk, B., Stringer, M. S., Koundal, S., MacIntosh, B. J., Rothman, D., & Benveniste, H. (2022). Choroid plexus tissue perfusion and blood to CSF barrier function in rats measured with continuous arterial spin labeling. *Neuroimage*, *261*, 119512. https://doi.org/10.1016/j.neuroimage.2022.119512

Lindner, T., Bolar, D. S., Achten, E., Barkhof, F., Bastos-Leite, A. J., Detre, J. A., Golay, X., Gunther, M., Wang, D. J. J., Haller, S., Ingala, S., Jager, H. R., Jahng, G. H., Juttukonda, M. R., Keil, V. C., Kimura, H., Ho, M. L., Lequin, M., Lou, X.,…on behalf of the, I. P. S. G. (2023). Current state and guidance on arterial spin labeling perfusion MRI in clinical neuroimaging. *Magn Reson Med*, *89*(5), 2024-2047. https://doi.org/10.1002/mrm.29572

Lokossou, A., Baledent, O., Garnotel, S., Page, G., Balardy, L., Czosnyka, Z., Payoux, P., & Schmidt, E. A. (2018). ICP Monitoring and Phase-Contrast MRI to Investigate Intracranial Compliance. *Acta Neurochir Suppl*, *126*, 247-253. https://doi.org/10.1007/978-3-319-65798-1_50

Mortazavi, S., Jamalipour Soufi, G., Rajabi, F., Akbaripour, S., Maracy, M. R., & Barekatain, M. (2022). Relationship between cognitive profile and neuroradiographic parameters in patients with idiopathic normal pressure hydrocephalus. *Curr J Neurol*, *21*(3), 178-182. https://doi.org/10.18502/cjn.v21i3.11111

Muangpaisan, W., Ngamsombat, C., Vichianin, Y., Dumrikarnlert, C., Seeboonruang, A., Pooliam, J., Charnchaowanish, P., Pongnapang, N., Kanjanapong, S., Phannarus, H., Pongmoragot, J., & Chawalparit, O. (2025). Brain Volume Metric Analysis Is Correlated with Aging Changes and Sex Differences in Thai Older Adults. *Dement Geriatr Cogn Dis Extra*, *15*(1), 47-57. https://doi.org/10.1159/000543774

Muir, R. T., Wang, S., & Warf, B. C. (2016). Global surgery for pediatric

hydrocephalus in the developing world: a review of the history, challenges, and future directions. *Neurosurg Focus*, *41*(5), E11. https://doi.org/10.3171/2016.7.FOCUS16273

Nakajima, M., Yamada, S., Miyajima, M., Ishii, K., Kuriyama, N., Kazui, H., Kanemoto, H., Suehiro, T., Yoshiyama, K., Kameda, M., Kajimoto, Y., Mase, M., Murai, H., Kita, D., Kimura, T., Samejima, N., Tokuda, T., Kaijima, M., Akiba, C.,…research committee of idiopathic normal pressure, h. (2021). Guidelines for Management of Idiopathic Normal Pressure Hydrocephalus (Third Edition): Endorsed by the Japanese Society of Normal Pressure Hydrocephalus. *Neurol Med Chir (Tokyo)*, *61*(2), 63-97. https://doi.org/10.2176/nmc.st.2020-0292

Owler, B. K., Momjian, S., Czosnyka, Z., Czosnyka, M., Pena, A., Harris, N. G., Smielewski, P., Fryer, T., Donovan, T., Coles, J., Carpenter, A., & Pickard, J. D. (2004). Normal pressure hydrocephalus and cerebral blood flow: a PET study of baseline values. *J Cereb Blood Flow Metab*, *24*(1), 17-23. https://doi.org/10.1097/01.WCB.0000093326.88757.49

Park, H. Y., Kim, M., Suh, C. H., Lee, D. H., Shim, W. H., & Kim, S. J. (2021). Diagnostic performance and interobserver agreement of the callosal angle and Evans' index in idiopathic normal pressure hydrocephalus: a systematic review and meta-analysis. *Eur Radiol*, *31*(7), 5300-5311. https://doi.org/10.1007/s00330-020-07555-5

Park, Y. S. (2022). Treatment Strategies and Challenges to Avoid Cerebrospinal Fluid Shunting for Pediatric Hydrocephalus. *Neurol Med Chir (Tokyo)*, *62*(9), 416-430. https://doi.org/10.2176/jns-nmc.2022-0100

Portella, G., Cormio, M., Citerio, G., Contant, C., Kiening, K., Enblad, P., & Piper, I. (2005). Continuous cerebral compliance monitoring in severe head injury: its relationship with intracranial pressure and cerebral perfusion pressure. *Acta Neurochir (Wien)*, *147*(7), 707-713; discussion 713. https://doi.org/10.1007/s00701-005-0537-z

Rosu, A. I., Andrei, D., Ghenciu, L. A., & Bolintineanu, S. L. (2025). Hydrocephalus: Molecular and Neuroimaging Biomarkers in Diagnosis and Management. *Biomedicines*, *13*(7). https://doi.org/10.3390/biomedicines13071511

Seltzer, L. A., Couldwell, M. W., Tubbs, R. S., Bui, C. J., & Dumont, A. S. (2024). The Top 100 Most Cited Journal Articles on Hydrocephalus. *Cureus*, *16*(2), e54481. https://doi.org/10.7759/cureus.54481

Shimony, N., Martinez-Sosa, M., Osburn, B., & Jallo, G. I. (2021). Non-traumatic pediatric intracranial hypertension: key points for different etiologies, diagnosis, and treatment. *Acta Neurol Belg*, *121*(4), 823-836. https://doi.org/10.1007/s13760-021-01626-0

van Swieten, J. C., Koudstaal, P. J., Visser, M. C., Schouten, H. J., & van Gijn, J. (1988). Interobserver agreement for the assessment of handicap in stroke patients. *Stroke*, *19*(5), 604-607. https://doi.org/10.1161/01.str.19.5.604

Virhammar, J., Laurell, K., Ahlgren, A., & Larsson, E. M. (2017). Arterial Spin-Labeling Perfusion MR Imaging Demonstrates Regional CBF Decrease in Idiopathic Normal Pressure Hydrocephalus. *AJNR Am J Neuroradiol*, *38*(11), 2081-2088. https://doi.org/10.3174/ajnr.A5347

Wang, Z., Zhang, Y., Hu, F., Ding, J., & Wang, X. (2020). Pathogenesis and pathophysiology of idiopathic normal pressure hydrocephalus. *CNS Neurosci Ther*, *26*(12), 1230-1240. https://doi.org/10.1111/cns.13526

Yeom, K. W., Lober, R. M., Alexander, A., Cheshier, S. H., & Edwards, M. S. (2014). Hydrocephalus decreases arterial spin-labeled cerebral perfusion. *AJNR Am J Neuroradiol*, *35*(7), 1433-1439. https://doi.org/10.3174/ajnr.A3891

Yushkevich, P. A., Piven, J., Hazlett, H. C., Smith, R. G., Ho, S., Gee, J. C., & Gerig, G. (2006). User-guided 3D active contour segmentation of anatomical structures: significantly improved efficiency and reliability. *Neuroimage*, *31*(3), 1116-1128. https://doi.org/10.1016/j.neuroimage.2006.01.015

Zhao, L., Taso, M., Dai, W., Press, D. Z., & Alsop, D. C. (2020). Non-invasive measurement of choroid plexus apparent blood flow with arterial spin labeling. *Fluids Barriers CNS*, *17*(1), 58. https://doi.org/10.1186/s12987-020-00218-z

Zhu, L., Stein, L. R., Kim, D., Ho, K., Yu, G. Q., Zhan, L., Larsson, T. E., & Mucke, L. (2018). Klotho controls the brain-immune system interface in the choroid plexus. *Proc Natl Acad Sci U S A*, *115*(48), E11388-E11396. https://doi.org/10.1073/pnas.1808609115

List of abbreviations

ASL	arterial spin labeling
CBF	cerebral blood flow
ATT	arterial transit time
sPH	secondary hydrocephalus
iPH	idiopathic hydrocephalus

Declarations

Ethics approval and consent to participate

The present work is based on the approved IRB 2025-k-301-01 by the Second Affiliated Hospital of Wenzhou Medical University in accordance with the Declaration of Helsinki. The consent to participates was waived in this retrospective study.

Consent for publication

The content of the manuscript has not been published submitted elsewhere.

Availability of data and materials

The present model will be provided online at github://xxx when the work is published. The datasets used during the current study are available from the corresponding author on reasonable request.

Competing interests

There is no conflict of interest from all the authors.

Funding

This work is supported by the National Key R&D Program of China (2023YFE0118900), the National Natural Science Foundation of China (32427802), and the Key Research and Development Program of Zhejiang Province China (2026C04037).

Authors' contributions

Z.Z., W.X., and Y.X. performed the data collection and data analysis. Y.J., P.P. and Z.L. performed the data collection and the protocol setting. W.D., Z.Y. and L.Z. provided the original idea, discussion of the results, and the fundings. All authors reviewed and approved the manuscript.

Author List

Zibo Zhou [1,3†]	17826721826@163.com
Weizhi Xia [1,3†]	kumamon1115@163.com
Yunzhi Xu [2]	12315033@zju.edu.cn
Yubin Jin [1,3]	15258781967@163.com
Peilong Pan [1,3]	ppl20010623@wmu.edu.cn
Zixuan Lin [2]	zixuan.lin@zju.edu.cn
Dan Wu [1,2]	danwu.bme@zju.edu.cn
Zhihan Yan [1,3*]	yanzhihanwz@163.com
Li Zhao [2*]	lz5bf@virginia.edu

1 Department of Radiology, The Second Affiliated Hospital and Yuying Children's Hospital of Wenzhou Medical University, Wenzhou, Zhejiang 325027, China.

2 Key Laboratory for Biomedical Engineering of Ministry of Education, College of Biomedical Engineering & Instrument Science, Zhejiang University, Hangzhou 310027, China

3 Wenzhou Key Laboratory of Structural and Functional Imaging, Wenzhou, 325027, China

†These authors contributed equally.

*Corresponding authors

Supplementary Files

This is a list of supplementary files associated with this preprint. Click to download.

- Supplementary.docx